Moritz Sieber, Christian Oliver Paschereit, Kilian Oberleithner

Impact of density stratification on the global mode in a swirling jet: Stochastic modelling and Lagrangian coherent structures

Citation details
Sieber, M., Paschereit, C. O., & Oberleithner, K. (2021). Impact of density stratification on the global mode in a swirling jet: Stochastic modelling and Lagrangian coherent structures. In International Journal of Heat and Fluid Flow (Vol. 90, p. 108820). Elsevier BV. https://doi.org/10.1016/j.ijheatfluidflow.2021.108820.

Impact of density stratification on the global mode in a swirling jet: Stochastic modelling and Lagrangian coherent structures

Moritz Sieber[a,b,*], Cristian Oliver Paschereit[b], Kilian Oberleithner[a]

[a] *Laboratory for Flow Instabilities and Dynamics, ISTA, Technische Universität Berlin*
[b] *Chair of Fluid Dynamics, ISTA, Technische Universität Berlin*

Abstract

In an experimental investigation, the stochastic dynamics of the global mode in a turbulent swirling jet are considered. From the application of the swirling jet in gas turbine combustors, it was observed that a specific density gradient in the flow leads to a suppression of the global mode. This phenomenon was replicated in a generic swirling jet using an electrical heating coil placed inside the breakdown bubble. In the present investigation, the dynamics of the global mode obtained from PIV and pressure measurements are analysed using a stochastic reduced-order model to describe the instability. The stochastic model is necessary to explain the interaction between the deterministic dynamics of the global mode and the perturbations by the background turbulence. The calibration of the stochastic model provides the amplification rate of the global mode that defines the transition of the flow, dependent on the swirling strength and the density difference. The spatial structure of the global mode is further investigated from Lagrangian coherent structures of the flow field which are computed from the 3D time-resolved velocity field reconstruction based on planar PIV measurements. The Lagrangian visualisations and schlieren visualisations are used to explain the absence of the density effects on the global mode at larger Reynolds numbers. The analysis gives a detailed view of the stochastic dynamics of a hydrodynamic instability in a turbulent flow.

Keywords: swirling jet, global mode, hydrodynamic instability, stochastic model, Lagrangian coherent structures, finite time Lyapunov exponent, flow visualisation

1. Introduction

A swirling jet denotes a class of circular jets that have a circular motion in addition to the axial motion of the fluid. It is widely used in gas turbine combustors due to a unique fluid dynamic feature called vortex breakdown [1]. The vortex breakdown manifests as a region of reversed flow in the centre of the jet [2]. In a swirl-stabilised combustor, the vortex breakdown stabilises the flame due to the recirculation of hot products and provides low velocities, which facilitates aerodynamic anchoring of the flame.

The swirling jet gives also rise to a global hydrodynamic instability that is controlled by the swirl intensity of the flow [3, 4, 5]. In combustion-related investigations, this instability is referred to as the precessing vortex core (PVC). The PVC is known to interact with the flame due to the mixing of reactants and stretching of the flame front [1, 6]. In reverse, the flame also influences the PVC which may lead to suppression or emergence of the PVC at certain operating conditions of a combustor [1, 7]. It has been shown that the combustion-induced density stratification in the shear layers leads to a suppression of the hydrodynamic instability [8]. Detailed experiments with a generic swirling jet were able to reproduce the phenomenon by mimicking the heat release of the flame by an electric heater [9, 10]. The combined experimental and numerical study showed that the amplitude of the PVC is strongly reduced, however, no complete suppression was attained experimentally. However, the appearance of the global mode in the data appeared to be in contradiction to the global instability of the mean flow as it was determined from a spatio-temporal stability analysis. As will be shown in this work, this contradiction can be resolved by considering the stochastic forcing of the global modes by turbulence.

In the present study, the dynamics of the global mode in the turbulent flow is modelled by a stochastic dynamical system. The model consists of a deterministic part that describes the oscillatory motion of the global mode and the leading nonlinearities that cause saturation at the limit cycle. Secondly, the model includes the perturbations by the background turbulence as a stochastic forcing. At stationary operation conditions, the flow tends to settle at a stable state or limit cycle. However, the turbulent perturbations continuously disturb the flow about that stable state. From the deterministic return to the stable state, the model can be calibrated. Therefore, the deterministic and stochastic dynamics are identified from the data and

*Corresponding author
Email addresses: moritz.sieber@fd.tu-berlin.de (Moritz Sieber), www.fd.tu-berlin.de (Cristian Oliver Paschereit), www.flow.tu-berlin.de (Kilian Oberleithner)

the model is adjusted to replicate thous. This requires only stationary, but time-resolved measurements of the flow.

The modelling approach adopted here was previously used to determine the deterministic characteristics of thermoacoustic oscillations in combustors [11, 12]. Furthermore, it was used to determine the bifurcation point of a hydrodynamic instability in a low-density jet from randomly forced measurements in the stable regime [13]. Moreover, the experimental observations of the PVC in an isothermal swirling jet were described in detail in a very recent investigation using the same stochastic approach [14]. In the present study, this work is extended to clarify the impact of heating on the global stability that causes the formation of the PVC.

The general difference of a stochastic model to a purely deterministic model is the possibility to capture dynamics in the flow that arise from linearly stable modes. Due to the stochastic forcing, stable modes of the flow get excited and require some time to decay again, which allows them to be observed in measurements. The level of the system oscillation depends on the intensity of the stochastic forcing. Almost periodic oscillations are observed in some systems, although caused by stochastic forcing, which is denoted as coherence resonance [15]. Such coherence resonances were observed in thermoacoustic systems [16, 17] and fluid dynamic systems [18].

An essential aspect for the understanding of fluid dynamics is not only the analysis of the temporal dynamics but also the investigation of the spatial structures. Therefore, schlieren images are recorded in this study making use of the density differences in this flow. The visual representation of a flow structure allows drawing an intuitive connection to the interaction between the stochastic turbulent fluctuations and the coherent structure. In the present investigation, the Schlieren images are further compared to Lagrangian coherent structures computed from the measured velocity fields[19]. For this purpose, a regularisation procedure is applied in combination with a reconstruction scheme to obtain a smooth 3D time-dependent representation of the flow field. The determined Lagrangian coherent structures allow a good comparison to the Schlieren-based flow visualisations and help to understand mixing phenomena [20, 21, 22]. Furthermore, the relation to instabilities of variable-density Kelvin-Helmholz instabilities is discussed [23, 24].

The paper is organised as follows. In section 2, the experimental and analytical methods are detailed. This comprises the description of measurement techniques, the identification of flow structure and the computation of Lagrangian coherent structures as well as the description of the stochastic model and the related calibration from the measurement data. The corresponding results for the mean flow field, different flow visualisations and calibration of the stochastic model are given in section 3. The findings obtained by the combined consideration from the different results are discussed in section 4. In section 5, the findings are summarised and discussed in light of previous related studies and swirl combustion applications.

2. Experimental and numerical methods

2.1. Experimental setup and measurement techniques

The flow of a generic swirling jet was investigated experimentally. The utilised setup is depicted schematically in figure 1. It consists of a radial swirl generator that is connected to a settling chamber followed by a contoured contraction. The flow emanates into the unconfined ambient, where the swirling jet evolves. The airflow into the swirler was set with a mass flow controller and the radial vanes in the swirler were adjusted with an automated stepper motor. The setup was utilised in previous investigations on the dynamics of the PVC under isothermal conditions [25, 26, 14] as well as with a heated breakdown bubble [9, 10, 21].

The breakdown region of the flow was heated by a loose wire coil that was directly exposed to the flow. It was made of a spirally wound 0.5 mm Nickle-Chromium wire (NiCr6015) and held in place by two thicker metal rods that also provided the electrical connection. The heating coil had a diameter of 20 mm and height of 43 mm. The coil was mounted such that the laser can pass between the two metal rods that hold the coil. A part of the laser light was reflected by a mirror to illuminate the part of the flow that was shadowed by the coil (figure 1). For the PIV measurements, a card mask with the shape of the coil was put between the coil and the camera to protect the chip from strong reflections. The coil was connected to an adjustable power supplied that was operated in constant current mode. The maximum operation current for the presented measurements was 4.6 A which corresponds to 165 W electrical power.

The coordinate orientation is indicated in the experimental setup in figure 1. The velocities in x-, y- and z-direction are given by v_x, v_y and v_z, which are commonly represented as vector $\boldsymbol{v} = [v_x, v_y, v_z]^T$. The origin of the coordinate system is located in the centre of the nozzle exit plane. The x-direction is aligned with the direction of gravity to avoid symmetry breaking. Furthermore, cylindrical coordinates are used given as $[x, r, \theta]$ that correspond to the Cartesian as $r = \sqrt{y^2 + z^2}$ and $\theta = \angle(y + iz)$.

The flow velocity was measured using stereoscopic particle image velocimetry (PIV) as sketched in figure 1. The three velocity components were measured in the x-y-plane right after the nozzle. Two 4 megapixel cameras with 50 mm lenses and a 150 mJ dual laser were used for the measurements. The flow was seeded with titanium oxide powder that was introduced into the flow between the mass flow controller and the swirler. However, the air supply for the seeder was split from the main lines downstream of the mass flow controller as shown in figure 1. For each configuration, a set of 1000 snapshots were recorded at a rate of 6 Hz. The images were processed with PIVview (PIVTEC

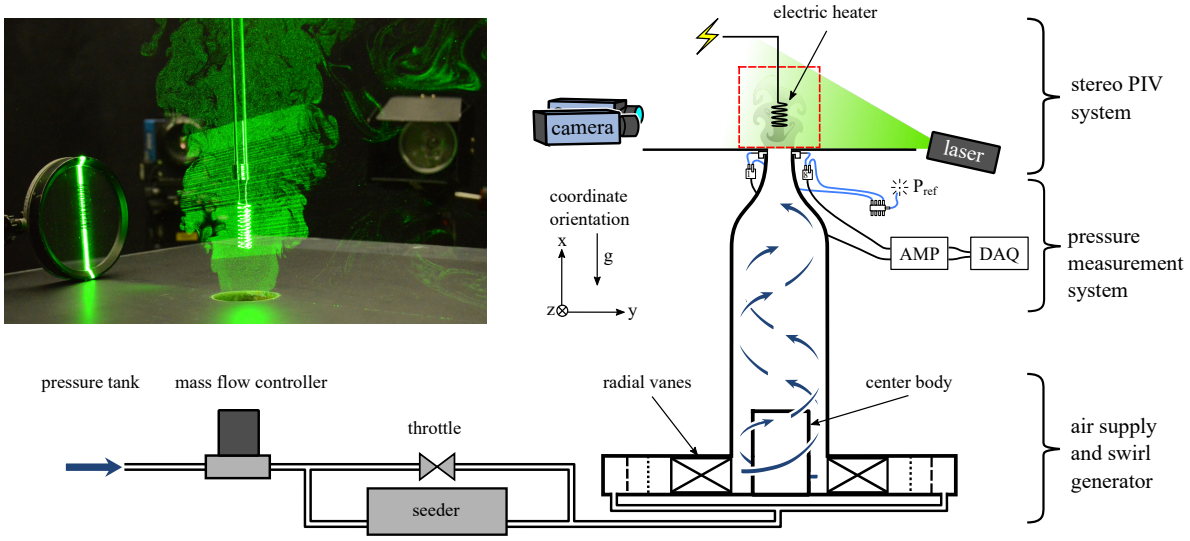

Figure 1: Schematic of the experimental setup together with the utilised measurement equipment. The red square marks the PIV measurement domain. The coordinate system is given next to the setup, the actual origin is in the centre of the nozzle exit plane. The photo shows the seeded jet and the heating coil, illuminated by the laser.

GmbH) using standard digital PIV processing [27]. Further details about the PIV measurement procedure can be found in Rukes et al. [25, 9].

Schlieren images of the flow were recorded with a Toepler Z-type setup with a knife-edge in x-direction [28]. Therefore, two identical mirrors with a focal length of 2.5 m were placed with an opening angle of approximately 15 °. The light, emanated from a white LED (10 mm diameter), was guided through the flow and recorded with a Nikon-3200 DSLR camera placed in the setup without a lens.

Around the circumference of the nozzle, eight pressure sensors were mounted to sense the PVC dynamics. Differential pressure sensors with a measurement range of 1000 Pa were used. The signals were amplified by in-house bridge amplifiers and recorded with 24 bit AD converters. Further details are given in Lang et al. [21] and Sieber et al. [14]. For each configuration, 180 s were recorded at a rate of 2 kHz. The data was digitally down-sampled at a rate of 100 Hz with an appropriate aliasing filter. At the investigated conditions, the measured pressure differences were of the order of 1 Pa. Therefore, the bridge amplifiers were set to high gain and high-resolution AD converters were used. Special care was taken to avoid electromagnetic interference by additional shielding of cables, mounting of ferrite cores, and proper grounding of all components. The power supply of the data acquisition and the amplifiers were isolated from the main grid by a coil transformer.

The temperature in the breakdown region was measured by a type-K thermocouple with 0.25 mm shaft diameter. It was traversed through the domain to record the mean temperature distribution in the flow. These measurements are further detailed in Rukes et al. [9] and Lang et al. [21].

2.2. *Operation conditions*

The heated swirling jet is characterised by the Reynolds number, swirl number and the density ratio. The Reynolds number is given as

$$\mathrm{Re} = \frac{v_{\mathrm{bulk}} D}{\nu} \quad \text{with} \quad v_{\mathrm{bulk}} = \frac{\dot{m}}{\rho_j \pi (D/2)^2}, \tag{1}$$

where $\dot{m}$ denotes the mass flow and $D = 51$ mm is the nozzle diameter. The density inside the breakdown bubble ρ_b relative to the jet density ρ_j defines the density ratio as

$$\rho^* = \frac{\rho_b}{\rho_j}\,. \tag{2}$$

Temperature measurements at an intermediate swirl number are used to calibrate a polynomial relation between the heating current and the density in the breakdown bubble, ρ_b. The reference density of the jet, ρ_j, is calculated from ambient conditions.

The swirl number S is assumed to be proportional to the swirler vane angle. This was confirmed in previous studies [25, 9, 14], where offset and proportionality are adjusted from the integral swirl number at some conditions. Accordingly, the integral swirl number obtained from the ratio of axial flux of azimuthal momentum to the axial flux of axial momentum is deduced from the swirler vane angle [14]. Compressibility effects and the influence of buoyancy are neglected due to the small Mach and Richardson numbers for the investigated conditions. With the definitions according to Rukes et al. [9], the Mach numbers are below 0.01 and Richardson numbers are below 0.05.

The PIV measurements were conducted for $\mathrm{Re} = 4000$ and $S = 0.98$ whereas ρ^* was varied in the range between 0.32 and 1. Measurements were conducted on three consecutive days whereby the entire range of density ratios was

measured repeatedly. For the pressure measurements, two sets were recorded at different Reynolds numbers. The measurements were conducted by an automated procedure, where the swirler vanes and heating current were changed. The corresponding parameter ranges are summarised in table 1. For both configurations, the swirl was increased in 9 steps and the density ratio was decreased in 21 steps. Each pressure measurement set was acquired during continuous operation of the facility for approximately 12 h. Schlieren visualisations were conducted for various Reynolds numbers, but only with mild heating and at a fixed swirl number.

2.3. Measurement data preprocessing

The PVC is identified from the PIV measurements using snapshot proper orthogonal decomposition (POD) [29]. Accordingly, the fluctuation part of the velocity field $\boldsymbol{v}' = \boldsymbol{v} - \overline{\boldsymbol{v}}$ is conceived as the modal decomposition

$$\boldsymbol{v}(x,t) = \overline{\boldsymbol{v}}(x) + \sum_{i=1}^{N} a_i(t)\boldsymbol{\Phi}_i(x)\,, \tag{3}$$

where a denotes the mode coefficients and $\boldsymbol{\Phi}$ the mode shape. Note that the bold symbols stand for vector quantities. The coefficients are obtained from the eigenvectors $\mathbf{a}_i = [a_i(t_1)\dots a_i(t_N)]^T$ of the snapshot correlation matrix $\mathbf{R}$ as follows

$$\mathbf{R}\mathbf{a}_i = \lambda_i \mathbf{a}_i, \quad \text{with} \quad R_{j,k} = \int \boldsymbol{v}(x,t_j)\boldsymbol{v}^T(x,t_k)\mathrm{d}x\,. \tag{4}$$

Further details on the application of POD to PIV data from swirling jets can be found in Oberleithner et al. [5] and Rukes et al. [25].

The PVC is commonly represented by the first two POD modes which can be combined to one complex-valued mode coefficient $A = a_1 + ia_2$. The PVC energy, in turn, results from the average squared magnitude $E = \overline{|A|^2}$.

For the stochastic modelling of the flow, long, time-resolved recordings of the PVC amplitude are necessary. These were obtained from the pressure measurements of the flow. From previous investigations, it is well established that the PVC mode can be deduced from circumferential pressure measurements [21, 26, 14, 30]. The pressure signals p_k recorded at eight azimuthal measurement positions were decomposed into azimuthal Fourier modes, reading

$$\widehat{p}_m(t) = \frac{1}{8}\sum_{k=1}^{8} p_k(t)\mathrm{e}^{-imk\pi/4}, \tag{5}$$

where m stands for the azimuthal wavenumber. The PVC was directly obtained as the first azimuthal mode $A = \widehat{p}_1$. The quality of the signal $\widehat{p}_1$ was furthermore improved by using a bandpass filter with the band $[\frac{2}{3}f_{\mathrm{PVC}}, \frac{3}{2}f_{\mathrm{PVC}}]$ centred around the average PVC frequency f_{PVC}, which was identified from the peak in the unfiltered spectrum. A second-order polynomial was fit to the region around the peak to estimate the frequency f_{PVC}. This was necessary for certain operation conditions, where the signal-to-noise level was very low. The pressure data were normalised by a factor of 0.1 Pa to have PVC amplitudes in the range 0 to 1.

2.4. 3D flow field reconstruction

This section describes the reconstruction of the 3D velocity field from PIV measurements, which is a preliminary stage for calculating the Lagrangian coherent structures. There are two essential steps, the estimation of the mode structure by phase averaging and the filtering of the data to retain the symmetries in the data and reduce measurement artefacts. The phase of the PVC is obtained from the argument of the complex amplitude, $\phi = \angle(a_1 + ia_2)$, where a_1 and a_2 are the coefficients of the two leading POD modes. This allows assigning a phase ϕ_k to each of the N PIV snapshot $\boldsymbol{v}_k$. Phase averaging is conducted according to the Fourier-averaging procedure described by [31]. Accordingly, the phase-averaged flow is represented as a Fourier series

$$\widetilde{\boldsymbol{v}}(\phi) = \sum_{n=-M}^{M} \widehat{\boldsymbol{v}}_n \mathrm{e}^{in\phi}, \tag{6}$$

where the Fourier coefficients are given as

$$\widehat{\boldsymbol{v}}_n = \sum_{k=1}^{N} \boldsymbol{v}_k \mathrm{e}^{-in\phi_k}. \tag{7}$$

The Fourier series is truncated after M modes to reject measurement noise. For real-valued input data, the positive and negative Fourier coefficients are the same $\widehat{\boldsymbol{v}}_n = \widehat{\boldsymbol{v}}_{-n}$. In contrast to common bin-based phase averaging, the Fourier-averaging allows the evaluation at arbitrary phases, which is relevant for the following reconstruction. Furthermore, the cut-off of the averaging in the frequency domain (fixed number of harmonics M) is more accurate than the selection of bin sizes and bin overlap [31]. In the current investigation, the mean ($n = 0$) and the first two harmonics, depicted in figure 2, are used to reconstruct the velocity field, which corresponds to $M = 2$. The least number of Fourier modes M that contribute to the phase averaged flow are found by inspecting the spatial structure of $\widehat{\boldsymbol{v}}_n$ and the decay of the L2-norm $||\widehat{\boldsymbol{v}}_n||$ with n.

In the present case, the oscillation in time is equivalent to a rotation about the symmetry axis of the jet. This is due to the swirling motion of the flow that couples axial and azimuthal phase velocities of the flow. Therefore, the azimuthal mode number m is equivalent to the temporal Fourier mode n. The coupling allows the reconstruction of the phase averaged 3D velocity field from a meridional measurement section [5]. Accordingly,

$$\widetilde{\boldsymbol{v}}(x,r,\theta,t) = \sum_{n=-M}^{M} \widehat{\boldsymbol{v}}_n(x,r)\mathrm{e}^{in(\theta-\omega t)}, \tag{8}$$

configuration	Re	S	ρ^*
PIV	4000	0.98	1 to 0.32
pressure 1	4000	0.81 to 1.15	1 to 0.40
pressure 2	6000	0.94 to 1.11	1 to 0.53
schlieren	1000 to 20 000	0.98	0.9

Table 1: Operation conditions for different measurement configurations.

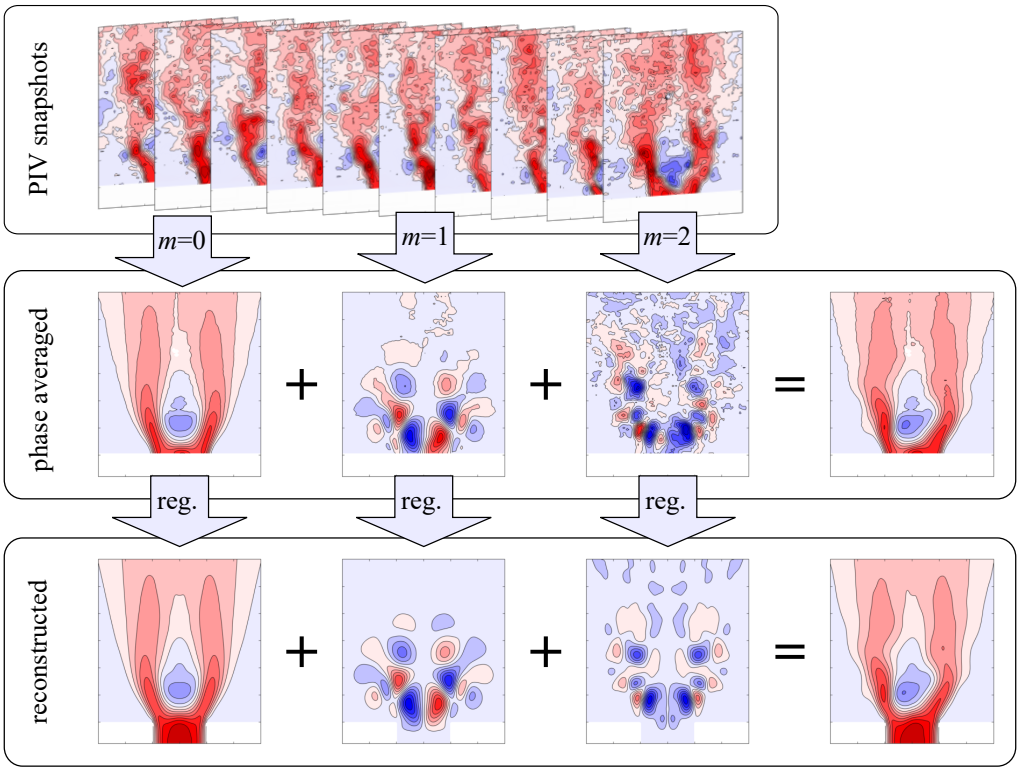

Figure 2: Schematics of the flow field reconstruction exemplified by the real part of the streamwise velocity component $\Re(v_x)$. The harmonic components $\widehat{\boldsymbol{v}}_n$ as well as their sum $\widetilde{\boldsymbol{v}}$ are presented (Re = 4000, $S = 0.98$, $\rho^* = 1$). The process involves phase averaging from the PIV snapshots and a regularisation (reg.) of the different Fourier components indicated by the azimuthal wavenumber m. The azimuthal mode number m is equivalent to the temporal harmonic n for the swirling jet.

where $[x, r, \theta]$ are the cylindrical coordinates.

For the reconstruction procedure, care has to be taken that the symmetry conditions are fulfilled at the jet axis. This is crucial as slight deviations are to be expected due to unavoidable misalignment of the measurement plane or imperfections in the experimental setup (see figure 2). Especially on the centre line, the symmetries between the left and right half, and also between the $\pi/2$ phase-shifted v_y and v_z components must match. The symmetries are restored by a subsequent filtering procedure that solves a constrained minimisation problem which fits a velocity field to the data. The numerical procedure is adopted from a surface fitting algorithm proposed by D'Errico [32], where a surface is fitted to elevation data with a regularisation penalty that controls the smoothness of the surface. The same approach is implemented for velocity data here, where additional constraints are included to satisfy the boundary conditions of the velocity field at the symmetry axis and the walls. Furthermore, constraints are included to fulfil the continuity equation. The thermal expansion in the vicinity of the coil is neglected since this region is not covered by the PIV and the reconstruction is only a coarse interpolation.

The velocity field reconstruction is carried out with the following steps. The velocity on the meridional plane of a regular polar grid $X = [v_x, v_r, v_\theta]$ is estimated from the measurements $Y = [v_x, v_y, v_z]$ on the x-y-plane. The misalignment and the match of the velocity component are handled by an interpolation operation $I(X) = Y$ that is implemented as a bi-linear interpolation. The interpolation is implemented as an implicit operation, which means that the data does not have to be available in a regular grid. The smoothness of the solution is controlled by a regularisation operator $R(X)$, which is the sum of the

second derivatives of the individual fields. The boundary conditions are adopted as Dirichlet or Neumann conditions with the operator $B(X) = Y_b$ and the continuity equation is represented as $C(X) = 0$. All operators are approximated as first-order finite differences. The velocity field is finally obtained by the minimisation of the combined problem

$$\min_X ||I(X) - Y||^2 + \lambda_R ||R(X)||^2 + \tag{9}$$

$$\lambda_B ||B(X) - Y_b||^2 + \lambda_C ||C(X)||^2, \tag{10}$$

where the parameters λ_R, λ_B and λ_C control the relative weighting of the individual constraints. The parameters are balanced by visual inspection of the solution. For the implementation of the continuity equation $C(X)$ in the polar coordinate system, the azimuthal mode number is considered, reading

$$\frac{\partial v_x}{\partial x} + \frac{\partial v_r}{\partial r} + \frac{1}{r} v_r + \frac{im}{r} v_\theta = 0. \tag{11}$$

The regularisation $R(X)$ is applied separately for each velocity and has the form (exemplified for v_x)

$$\frac{\partial^2 v_x}{\partial x^2} + \frac{\partial^2 v_x}{\partial r^2} = 0. \tag{12}$$

The approach provides smooth and reasonable velocity fields for each of the harmonics as presented in figure 2. The velocity field is also extrapolated into the nozzle, where no measurements were possible. This is helpful to allow reasonable computation of Lagrangian coherent structures near the nozzle. Moreover, the data are restored in the region of the heating element, where no measurement data were recorded. The removal of measurement uncertainties and the restoration of the symmetry of the flow provides a much better foundation for the computation of Lagrangian coherent structures than taking a simple phase average. Especially the uncertainties at the jet axis would otherwise create nonphysical artefacts.

2.5. Lagrangian coherent structures

The Lagrangian coherent structures are computed from the finite-time Lyapunov exponents (FTLE) [19]. The FTLE is a measure for the divergence of path lines in a fixed time interval, which can be calculated forward or backwards in time. Forward time FTLE highlights repelling structures whereas backward time FTLE pronounces attracting structures. In the present study, the interfaces between the jet and the breakdown bubble are investigated. These correspond to interfaces where the flow from different regions meet, which is highlighted by the backward time FTLE.

The different steps towards the FTLE representation of the flow are graphically summarised in figure 3. The basis for the computation of the FTLE is a 3D time-resolved representation of the flow field as it was determined from the procedure described in the previous section. To compute the FTLE, the flow is homogeneously seeded with virtual particles $\boldsymbol{x}_p$. The pathlines of these particles are computed backward in time from the velocity, reading

$$\boldsymbol{x}_p(t_0 - \Delta t) = \boldsymbol{x}_p(t_0) - \int_{t_0}^{t_0 - \Delta t} \widetilde{\boldsymbol{v}}(\boldsymbol{x}_p(t), t) \mathrm{d}t. \tag{13}$$

The integral is calculated with a 4th order Runge-Kutta solver and the integration time is chosen to be 1.5 periods of the PVC oscillation. The actual FTLE is calculated from the distance of particles after the integration relative to their initial distance. This is given by

$$\sigma_{\mathrm{FTLE}} = \frac{\log(d_0/d_1)}{\Delta t}, \tag{14}$$

where d_0 is the initial distance and d_1 the final distance after the integration time Δt. The divergence at one point is computed from a group of four particles, separated by a very small initial distance d_0 in all three coordinate directions. Since the divergence of pathlines is not homogeneous in all spatial direction, the maximal separation of the initial quadruplet of points is determined from the leading eigenvalue of the space spanned by the final distances between the points.

2.6. Stochastic modelling

To describe the observed dynamics of the PVC, Landau's amplitude equation is used [33]. The stochastic perturbations induced by turbulence are included as additive noise. The corresponding derivation of the governing equations and their application in the context of the PVC are detailed in Sieber et al. [14]. For brevity, only the main steps leading to the equations required for the analysis in the current study are summarised here. The utilised amplitude equation with additive noise reads as

$$\dot{A} = (\sigma + i\omega) A - \alpha |A|^2 A + \xi. \tag{15}$$

It describes the evolution of the complex-valued amplitude A forced by complex-valued additive noise ξ. The first term on the right hand side contains the frequency $\omega = 2\pi f_{\mathrm{PVC}}$ and the linear growth-rate σ of the PVC mode. The second term reflects the nonlinear saturation of the PVC at the limit cycle that is governed by the Landau constant α. In this investigation only real-valued α are considered, which neglects changes of the oscillation frequency due to the saturation (see also [14] for further details). The third term contains the stochastic forcing ξ, which is characterised by the autocorrelation

$$\langle \xi(t), \xi(s) \rangle = \frac{D_\xi}{\tau} e^{-|t-s|/\tau}. \tag{16}$$

The added noise depends on the noise intensity D_ξ and the noise time scale τ. This is coloured noise that coarsely considers the spectral decay of turbulence. In the derivations in [14] it was shown that it is also feasible to consider

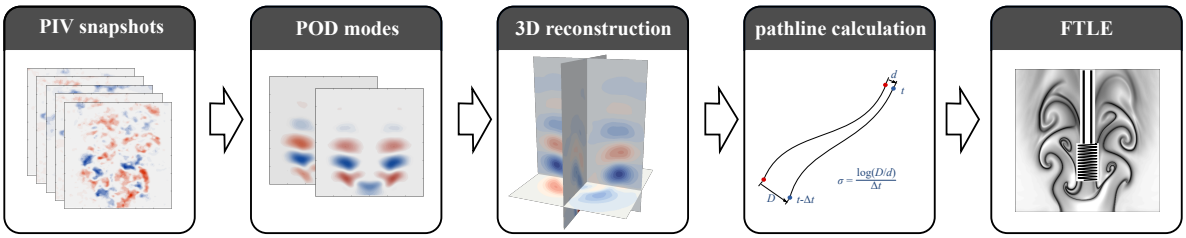

Figure 3: Flowmap depicting the steps from PIV measurements to the finite time Lyapunov exponents (FTLE).

this similar to white noise with an effective noise intensity, which is further detailed below.

By changing the variables to phase and magnitude, with $A = |A|e^{i\phi}$, and by subsequent stochastic averaging [34], a separation of equation 15 into magnitude and phase is achieved, reading

$$|\dot{A}| = \sigma|A| - \alpha|A|^3 + \frac{\Gamma}{|A|} + \xi_A \quad \text{and} \quad \dot{\phi} = \omega_0 + \frac{\xi_\phi}{|A|}, \tag{17}$$

respectively. In this representation, two uncorrelated, real-valued noise contributions ξ_A and ξ_ϕ are used which have half the variance of the complex-valued noise ξ. This allows the dynamics of the magnitude $|A|$ to be described independently from the phase. However, due to the stochastic forcing, another deterministic contribution is added to the equation that is governed by the effective noise intensity Γ.

The effective noise intensity Γ corresponds to the power spectral density of the noise at the oscillation frequency which is given by

$$\Gamma = \frac{2D_\xi}{\tau^2\omega^2 + 1}. \tag{18}$$

This considers the effect of the coloured noise forcing by introducing an equivalent white noise forcing with matching intensity. The simplified consideration of coloured noise by an effective noise intensity is only strictly valid if the noise time scale τ is smaller than the oscillation period $1/\omega$, leading to $\tau^2\omega^2 < 1$ [14].

The derivation based on Landau's amplitude equation shares some similarities with related stochastic equations based on the Van der Pol oscillator [11, 13]. As demonstrated in [14] the approaches differ mainly in the occurrence of a $\frac{1}{\omega}$ factor at the noise induced deterministic contribution $\frac{\Gamma}{|A|}$ in equation (17).

From equation (17), the stationary solution for the probability density function (PDF) of the magnitude $P(|A|)$ is derived, which has the following form

$$P(|A|) = \mathcal{N}|A| \exp\left(c_1|A|^2 + c_2|A|^4\right) \tag{19}$$

with the unknown parameters c_1 and c_2. The parameter $\mathcal{N}$ is chosen such that the integral PDF is normalised as $\int_0^\infty P(|A|) = 1$. The analytical solution (19) is fit to the measured PDF to estimate the unknown model parameters. The physical parameters of the amplitude equation (15) depend on these model parameters as

$$\sigma = \frac{c_1\Gamma}{2} \quad \text{and} \quad \alpha = -c_2\Gamma, \tag{20}$$

which includes an additional dependence on the added noise. To estimate the noise intensity from the experimental data, the phase equation (17) is rearranged to

$$\xi_\phi = |A|\left(\dot{\phi} - 2\pi f_{\mathrm{PVC}}\right), \tag{21}$$

which provides an estimate of the stochastic forcing that can be determined from the measured phase distortion of the PVC ξ_ϕ. The comparison of the autocorrelation of the estimated forcing $\langle\xi_\phi(t), \xi_\phi(s)\rangle$ to the theoretical function (16) allows the noise parameters D_ξ and τ to be determined, which in turn yields the effective noise intensity Γ (18).

Further details about the stochastic model and the related derivations are found in the investigation by Sieber et al. [14].

3. Results

The results are divided into two groups according to the experimental parameters. The PIV and flow visualisations are all conducted for a fixed swirl number of $S = 0.98$ and Reynolds number of $\mathrm{Re} = 4000$, whereas the pressure measurements span a larger range of swirl numbers. Therefore, the mean flow field and the mode structure obtained from POD, FTLE, and schlieren images are presented first. This is followed by the presentation of the stochastic model calibration based on pressure measurements.

3.1. Mean flow and temperature field

The basic characteristics of the flow field of a swirling jet undergoing vortex breakdown are illustrated in the sketch in figure 4 a. It shows the breakdown bubble that forms the annular jet with inner and outer shear layers. The shape of the dominant coherent structure, sketched in figure 4 b, is indicating that the vortex centre of the swirling jet precesses and wraps around the recirculating region. Due to this phenomenon, this coherent structure is termed the preprocessing vortex core (PCV). The roll-up of the vortices in the inner and outer shear layer due to Kelvin-Helmholtz-instability is synchronised with the motion of

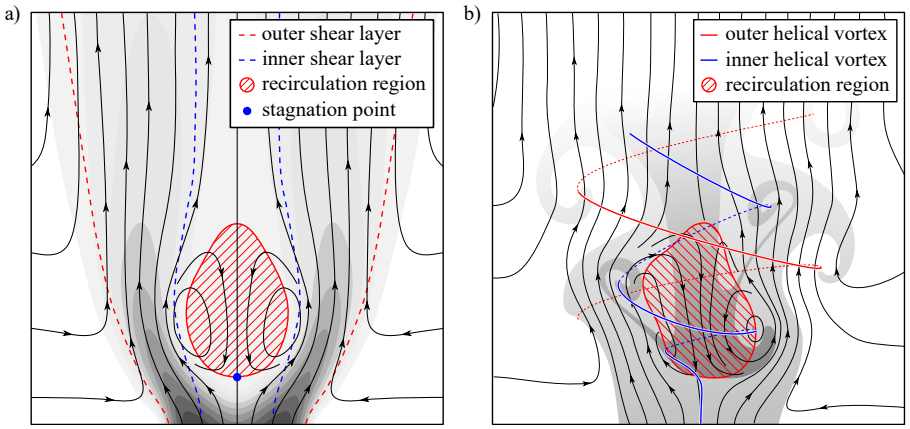

Figure 4: Schematics of the flow field: a) mean velocity field indicated by streamlines and velocity magnitude as grey contour levels, b) instantaneous velocity field indicated by streamlines and coherent structure as grey background. Specific features of the flow fields are marked and indicated in the legends. The breakdown bubble is indicated by the recirculating flow in the centre of the jet.

the vortex core. As indicated in the figure, the PVC motion causes a strong deformation of the breakdown bubble.

The shape of the mean flow field is further quantified in figure 5 based on the PIV data. The displayed axial velocity contours allow the backflow in the recirculation bubble to be compared to the velocity in the annular jet. In figure 5 a, it is visible that the magnitude of the backflow is approximately a third of the bulk velocity. Furthermore, the comparison of the velocity field without a coil (figure 5 a) and the field with an unheated coil inserted in the flow (figure 5 b) allows to quantify the influence of the coil on the mean flow. It shows that the velocity field outside of the coil is barely altered. Mainly, the breakdown bubble has become a little wider with the coil. However, a large part of the recirculating flow is guided through the coil which was the reason to place it there. Hence, the coil heats the backflow in the bubble and creates a density jump at the interface between the jet and the breakdown bubble.

The flow field with a heated coil is shown in figure 5 c. It shows that the heating does not change the overall characteristics of the flow. However, the considerable amount of heating applied in this case causes a decrease in the width of the breakdown bubble. The backflow has still a similar magnitude as observed for the cold case. This underlines the neglect of buoyancy effects due to the small Richardson numbers [9].

The mean temperature field is exemplified in figure 6 as a horizontal and vertical profile for the same case as shown in 5 c. Accordingly, the applied heating causes a strong temperature gradient in the inner shear layer. The slope of the temperature gradient in y-direction is opposite to the radial gradient of the axial velocity, which is decisive for the suppression of the PVC considered here. The maximum temperature at $x/D = 0.6$ and $y/D = z/D = 0$ is taken as reference for the density ratio introduced in equation (2). A more detailed discussion of the mean and phase averaged temperature field can be found in a related study, where the temperature field was reconstructed using tomographic background oriented schlieren [21].

3.2. POD mode shapes and energy

The POD was applied as the first measure to quantify the impact of the heating on the PVC. The display of the energy in figure 7 a shows that the heating strongly reduces the PVC energy as determined from the POD. However, a reduction is only prevailing until a density ratio of $\rho^* = 0.65$. Below that, there is only a marginal decay. Moreover, it is only reduced at maximum to 40 % of the energy in the cold case. With one exception, these observations are consistent with the earlier studies presented in Rukes et al. [9]. Previously, a slight increase in energy at low heating was observed. This was not reproduced in the present case although many repeated PIV measurements were undertaken in the present investigation (58 measurements). The variance of the results indicates that there is an intrinsic variance in the slow time scales in the order of minutes (PIV measurements are averages from approximately 3 min). This was also discussed in the context of the temperate field tomography in Lang et al. [21]. Therefore, the previously observed increase in energy at slight heating was most probably due to a variance of the experimental boundary conditions.

Figure 7 b shows the PDF of the PVC amplitude. Accordingly, the variance of individual snapshots is larger than the relative change of the mean value due to the changing density ratio. This explains the large variance of individual PIV measurements as indicated by the grey surface in figure 7 a.

The POD mode shape of the PVC is presented in figure 8, again showing cases without the coil, with unheated coil, and with the heated coil. The display of different cases shows again that the insertion of the unheated coil does not alter the flow significantly. The presented spatial structures for both cases agree nearly perfectly, except for a slight change in magnitude directly below the coil. More-

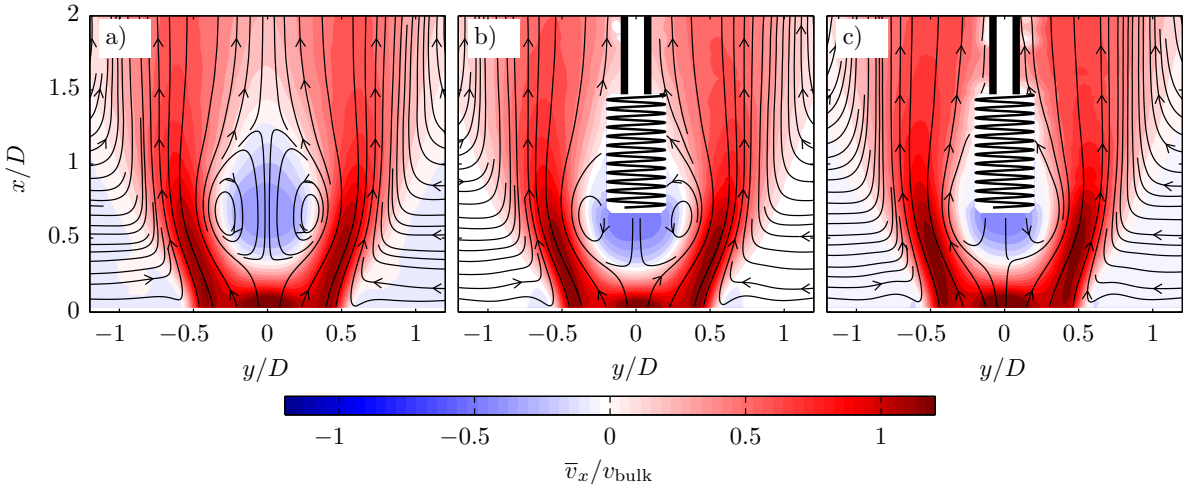

Figure 5: Mean velocity field for the baseline case a), flow with unheated coil $\rho^* = 1$ b) and heated flow $\rho^* = 0.5$ c) (Re = 4000, $S = 0.98$).

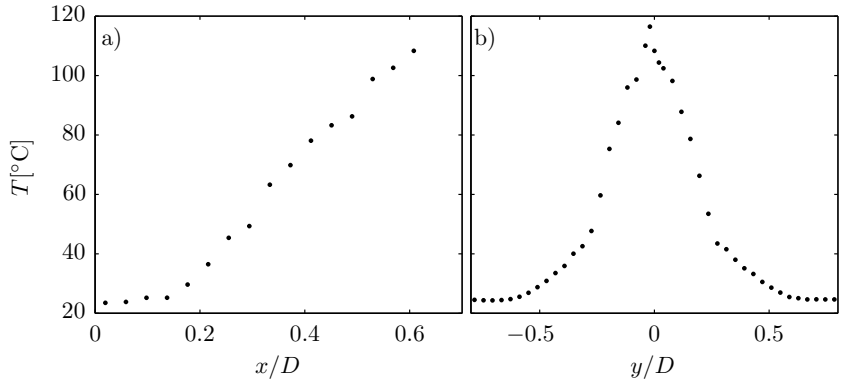

Figure 6: Measured mean temperature profiles a) along the centerline ($y = z = 0$) and b) along a crosswise profile below the heating coil ($x/D = 0.6$ $z = 0$) ($\rho^* = 0.8$, Re = 4000, $S = 0.98$).

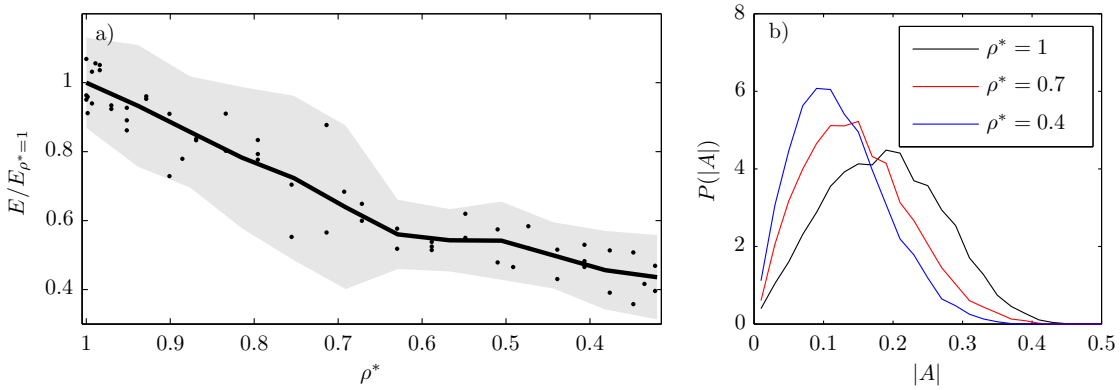

Figure 7: Energy of the PVC for decreasing density ratios a) and PDF of the oscillation magnitude b). a): The dots correspond to the mean energy from single PIV measurement with 1000 images each. The line and the gray surface mark estimates for the mean value and the 95% percentile respectively. b): The PDF constitutes the ensemble of PIV measurements in the range of $\Delta\rho^* = 0.06$ around the value indicated in the legend. (Re = 4000, $S = 0.98$).

over, the heating of the flow (figure 8 c) does also not have a visible impact on the mode shape.

The combined information from mode energy and mode shape indicates that the heating of the breakdown bubble roughly halves the PVC energy but does not change the spatial structure. This is important, as a systematic study of the influence of heating on PVC and modelling does not work if the heating alters the mean flow or the PVC mode shape.

3.3. Visualisation of the spatial structures

The spatial structure of the PVC is visualised from FTLE and schlieren images. The different approaches are compared to validate the extensive processing of the measurement data during the calculation of the FTLE. Furthermore, the schlieren images, which are instantaneous and not phase-averaged, provide insight into the small-scale turbulent mixing in the presented case.

The FTLE images for the baseline case, as well as the one with an unheated and heated coil, are presented in figure 9. The spatial structure of the FTLE is also sown in the sketch in figure 4, which allows a direct assignment to the vortex structures presented there. The deformed interfaces of the inner and outer shear layer are well visible from the FTLE. Furthermore, the synchronised roll-up of both shear layers in counter-rotating pairs becomes precisely visible. Whereby the vortex in the inner shear layer leads in streamwise position and magnitude. The general perception from the comparison of the three visualisations (figure 9 a-c) is that the insertion of the coil does not affect the structure and that the heating reduces the strength of the shear layer roll-up. This agrees well with the observations of the mode energy and mode shape in the previous section.

In figure 10 different experimental flow visualisations are presented. These show remarkable similarities with the FTLE visualisations in figure 9. The roll-up intensity and staggering of vortices at the two interfaces agree very well. The experimental visualisations represent a snapshot of a flow instance that is deliberately selected due to the good agreement with the other visualisations. Note that there is typically a phase-jitter in the experiment that disrupts the spatial arrangement of the structures, which is also visible from the downstream dispersion of the structures. The experimental flow visualisations are carried out at halve the Reynolds number to reduce the present distortions as far as possible. The FTLE images, instead, constitute idealised representations of the flow structures, where phase jitter is eliminated due to the phase averaging involved in the data processing. The qualitative agreement with experimental flow visualisations shows that the FTLE based on a low order reconstruction of the flow is a good approach to capture the essential features of the dominant coherent structure.

The Schlieren visualisations are further used to investigate the influence of an increased Reynolds number on the density stratification between the jet and the breakdown bubble. Figure 11 shows schlieren images of the flow around the heating coil for increasing Reynolds number. The selected snapshots show qualitative changes that are visible in all images for a specific Reynolds number. At Re = 4000 (Figure 11 a), there is a very sharp interface between the jet and the breakdown bubble around the stagnation point (see figure 4 a). With an increase to Re = 10 000 and Re = 20 000 (Figure 11 b and c), this interface becomes increasingly dispersed due to the turbulent diffusion of the small-scale structures. The flow still exhibits the same large-scale structures concerning the convective transport of heated air, however, the density gradient at the interface becomes blurred. The large scale structures are governed by the mean flow that is relatively unaffected by the Reynolds number changes, while the small-scale structures scale with the Reynolds number due to a reduction of the viscous effects. This observation will be important for understanding the mixing process involved in the current experiments.

3.4. Calibration of the stochastic model from pressure measurements

In the following, the calibration of the stochastic model using pressure measurement data are explained and the estimated model parameters for different operating conditions are presented.

To ease the understanding of the basic approach, we first consider a measured time series and the corresponding stationary PDF of the oscillation magnitude. In figure 12, the PVC amplitudes determined from the pressure signal according to equation 5 are presented for different swirl numbers. Strong modulation of the oscillation amplitude is evident for all conditions. The envelope of the oscillation further shows that the magnitude of the oscillation increases with swirl and the variance changes substantially. This can be even better inspected from the amplitude PDF shown next to the time series. At the lowest swirl number (figure 12 b), the PDF is similar to a Rayleigh distribution, while at the highest swirl number (figure 12 f) it is similar to a Gaussian distribution. For the intermediate swirl (figure 12 d) the PDF resembles a mixture of both distribution types.

To calibrate the model the analytical function (19) must be fitted to the measured PDF. This is done for different S and $\rho*$ to investigate the stability of the PVC depending on the operating conditions. Figure 13 a shows that this approximation is in good agreement. The changes in the PDF for different swirl numbers are further detailed in figure 13 b. It shows a continuous change of the PDF starting with narrow, low amplitude distributions, which increase in width and amplitude for increasing swirl intensity. The change from a Rayleigh to a Gaussian distribution, which was already observed in figure 12, is also visible. The fit to the experimental data is further conducted for all the investigated operation conditions to obtain the growth rate

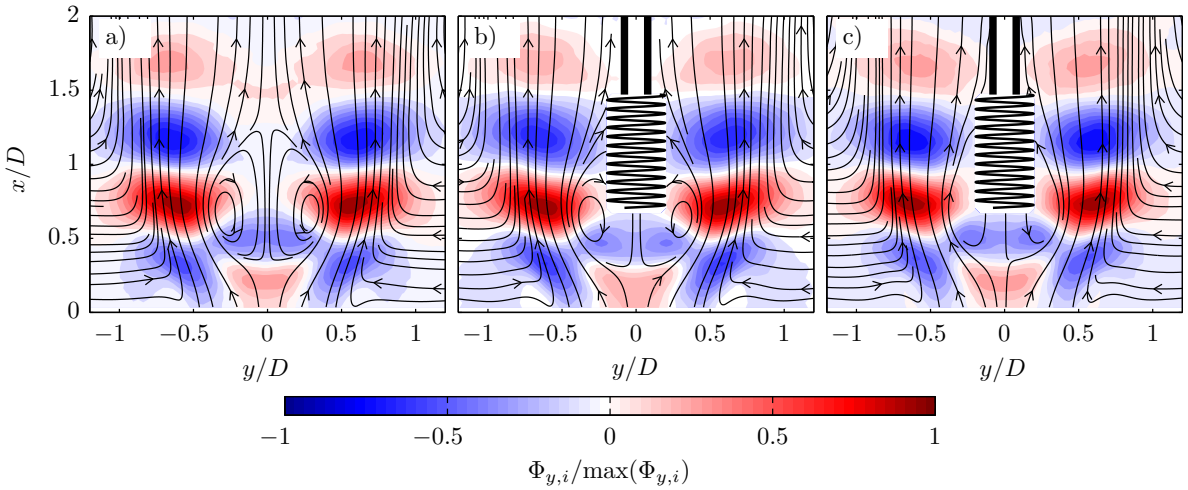

Figure 8: Leading POD mode for the baseline case a), flow with unheated coil $\rho^* = 1$ b) and heated flow $\rho^* = 0.5$ c). The phases of the modes are aligned to facilitate a comparison of the structure (Re = 4000, $S = 0.98$).

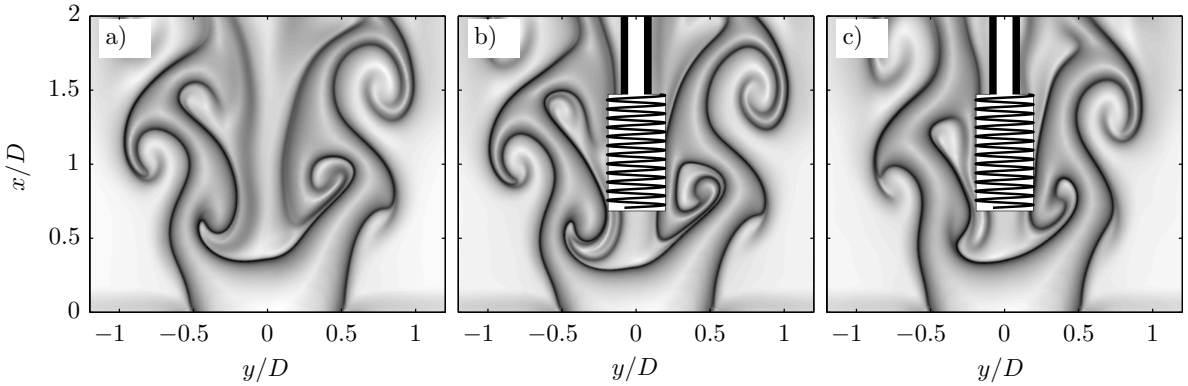

Figure 9: FTLE of the phase averaged flow for the baseline case a), flow with unheated coil $\rho^* = 1$ b) and heated flow $\rho^* = 0.5$ c) (Re = 4000, $S = 0.98$).

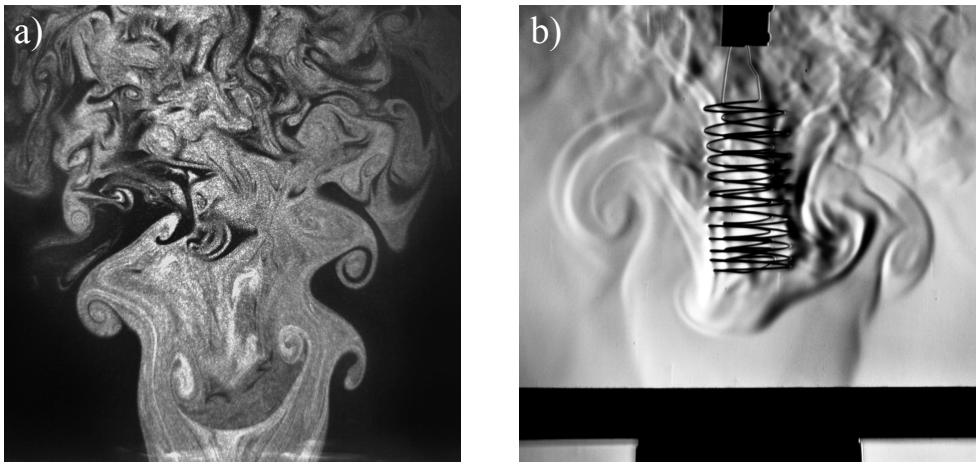

Figure 10: Smoke a) and Schlieren b) visualisation of the swirling jet at Re = 2000. For the smoke visualisation, the jet is seeded with oil particles and illuminated by a laser sheet. For the schlieren visualisation, the jet is heated slightly above the ambient temperature and the breakdown bubble is heated additionally by the coil ($S = 0.98$).

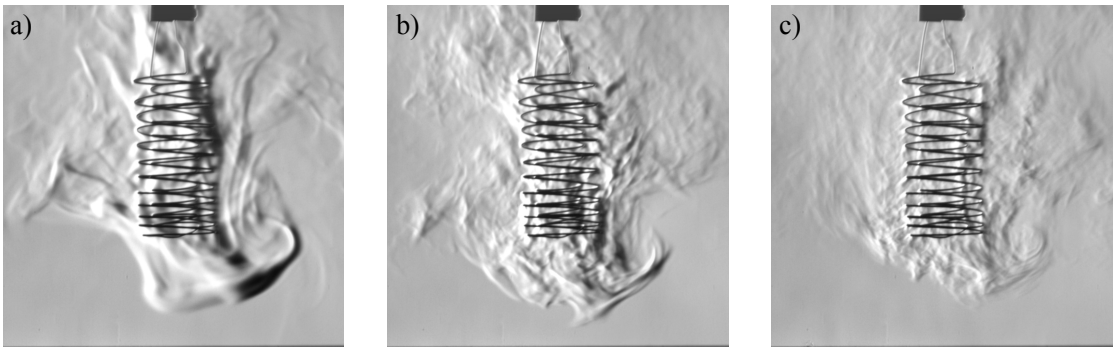

Figure 11: Schlieren visualisation of the heated breakdown bubble for increasing Reynolds numbers: a) Re = 4000, b) Re = 10 000, c) Re = 20 000. Similar phases of the global mode for different Re are selected according to visual similarity. Images are taken at slightly heated conditions $\rho^* \approx 0.9$ ($S = 0.98$).

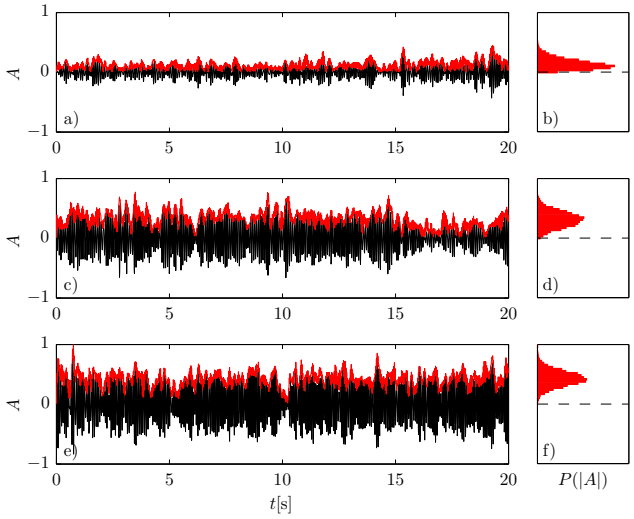

Figure 12: Time series of the PVC amplitude determined from the pressure Fourier coefficient $A = \widehat{p}_1$ (a,c,e) and probability density of the envelope $|A|$ (b,d,f) for increasing swirl numbers at $S = 0.98$ (a,b), $S = 1.06$ (c,d) and $S = 1.15$ (e,f). The black lines show the real part of the signal $\Re(A)$ and red lines and bars indicate the magnitude $|A|$ (Re = 4000, $\rho^* = 1$).

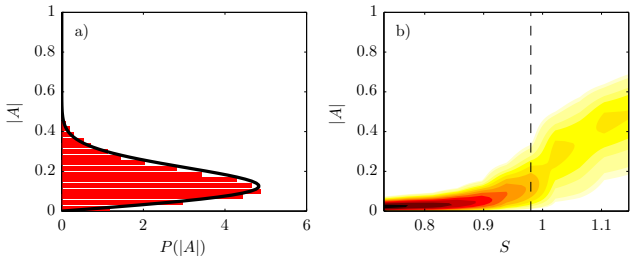

Figure 13: Probability density of the envelope $|A|$ at $S = 0.98$ together with the analytical fit (a) and fit of the probability density for increasing swirl numbers as contour plot (b). The dashed line indicates the position of the curve in plot a) (Re = 4000, $\rho^* = 1$).

of the PVC according to equation (20) as a function of swirl number and density ratio.

In figure 14 d, the amplification rate determined from the model is shown for all investigated swirl numbers and density ratios for Re = 4000. The stability margin, where the flow changes from negative to positive amplification rate is highlighted by a thick contour line. Furthermore, the mean magnitude, frequency and noise intensity are represented together with the stability margin (figure 14 a-c). In this representation, the frequency and amplification rate are normalised by the bulk velocity and nozzle diameter given by $\mathrm{St} = f u_{\mathrm{bulk}}/D$ and $\sigma^* = \sigma u_{\mathrm{bulk}}/D$. The data for the contour graphs are filtered in the S-ρ^*-plane by a 3×3 Gaussian filter to facilitate the visibility of contour lines and the perception of trends in the data. The same procedure applies for the analogue representation of the data at higher Reynolds numbers given in figure 15.

Figure 14 shows that the stability margin of the PVC mainly depends on the swirl number. At the lower Reynolds number (figure 14), the stability margin is inclined towards lower swirl numbers at isothermal conditions. This confirms a dependency of the flow instability on the density ration. There is a PVC magnitude level that coarsely coincides with the stability margin, which indicates that the amplitude of the instability is linked to the instability growth rate. However, the contours show that even at stable conditions there is still a substantial

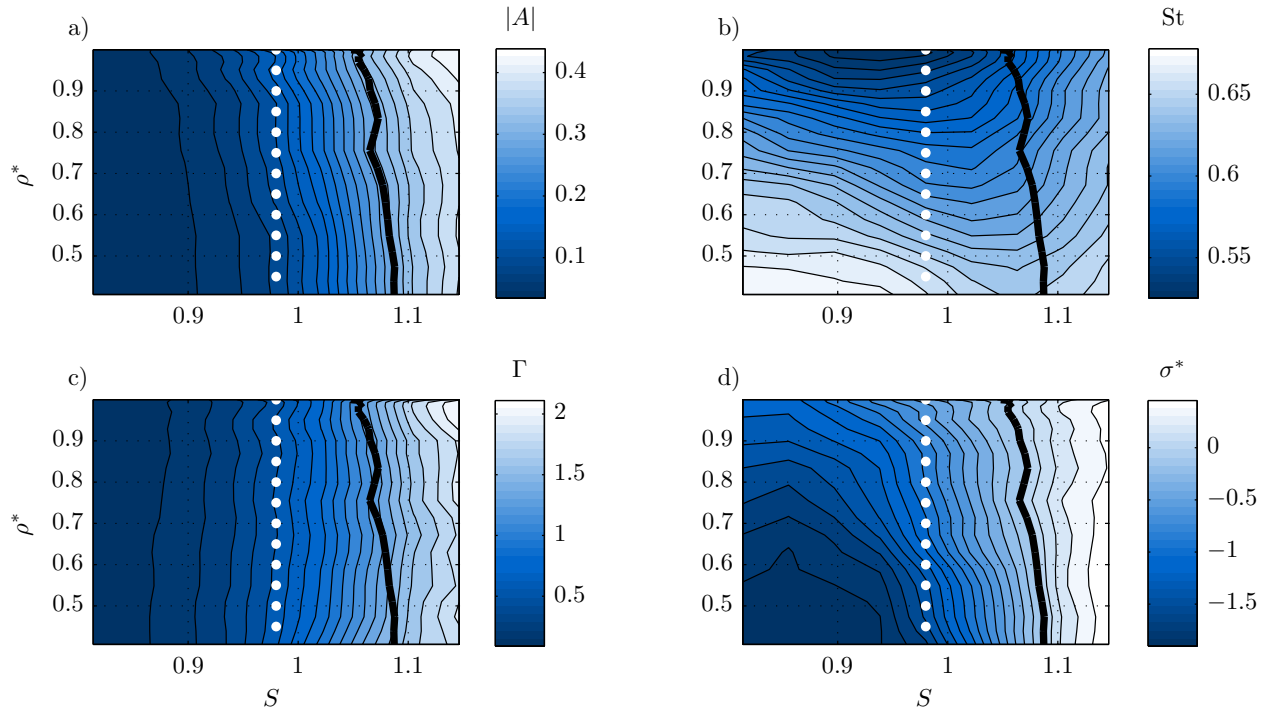

Figure 14: Calibration of the low dimensional model for changing swirl numbers S and density ratios ρ^* for Re = 4000. The contour plots show levels of the PVC amplitude $|A|$ a), normalised frequency St b), noise level Γ c) and normalised amplification rate σ^* d). The black line indicates the stability margin that separates the stable (left) and unstable (right) region in the parameter space. The white dots indicate the parameters of the PIV measurements in figure 7.

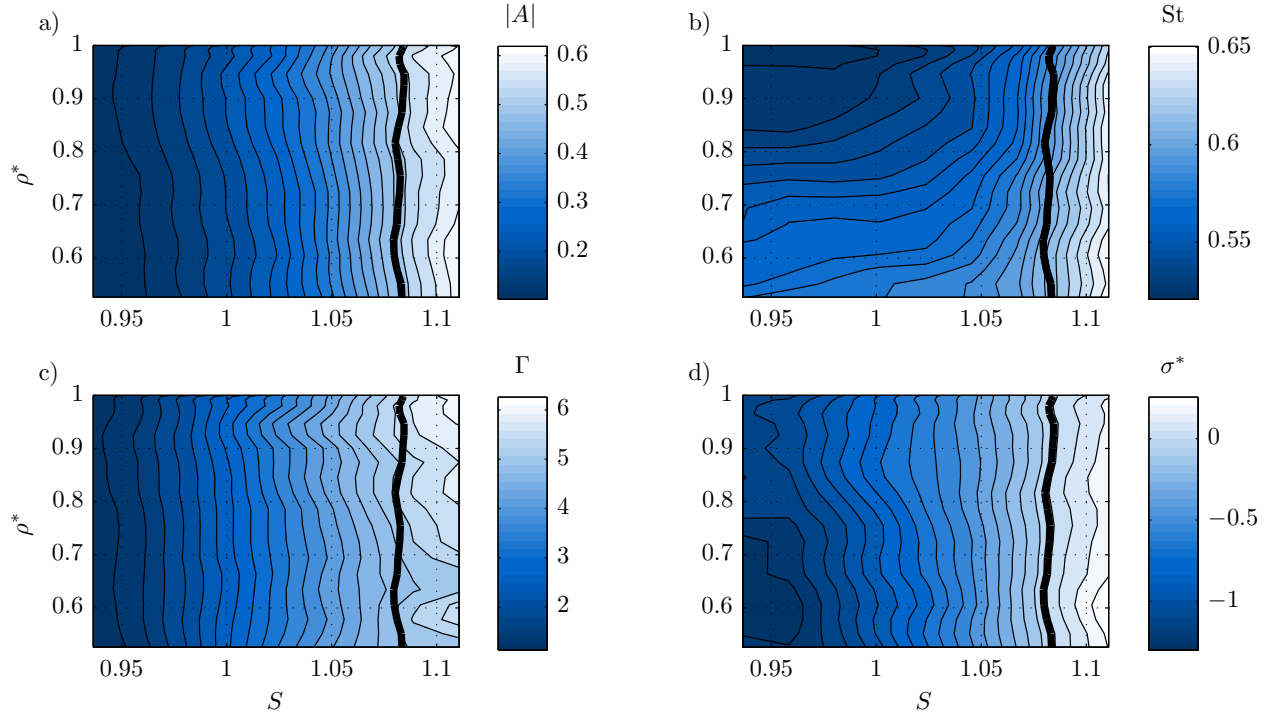

Figure 15: Same as fig. 14 but for Re = 6000.

PVC amplitude, which clearly shows the influence of the stochastic forcing. Furthermore, no indication of a bifurcation is visible from the magnitude.

The PVC frequency (figure 14 b) increases with swirl number and with decreasing density ratio. The increase at low swirl numbers and low-density ratios must be evaluated carefully since the signal level in this range are very low ($|A| < 0.1$). The effective noise, shown in figure 14 c, which is perturbing the PVC dynamics, scales mainly with the swirl number. Similar to the magnitude, it shows a continuous increase in the investigated range. The amplification rate (figure 14 d), however, shows a clear dependency on the density ration. Besides the inclination of the stability margin, the increase of the amplification rate with the swirl number becomes much steeper for reduced density ratios.

Figure 15 shows the identified model parameters for the higher Reynolds number. Accordingly, the dependency of the model parameters on the swirl stays very similar to the low Reynolds case, whereas the density ratio dependency has weakened or disappeared. The amplification rate (figure 15 d) still shows a steeper increase with the swirl number for lower density ratios, however, the stability margin does not depend on the density ratio. The frequency (figure 15 b) is also increasing slightly with decreasing density ratio. The amplitude (figure 15 a) and the effective noise (figure 15 c), however, depend only on the swirl number. It can be seen that by increasing the Reynolds number, the critical swirl number has not changed, but the influence of the density ratio becomes very small.

4. Discussion

The different aspects revealed from the combined consideration of the presented results are discussed in the following. This primarily concerns the influence of the Reynolds number on the stability margin of the PVC. Second, the relevance of the FTLE images and the related low-order representation of the flow for mixing is discussed. Finally, the impact of the stochastic dynamics in a turbulent flow on the experimental observations is explained.

4.1. Influence of the Reynolds number on the PVC suppression

The investigation at higher Reynolds numbers does not reveal a significant influence of the heating on the PVC. This is in line with previous observations by Rukes et al. [9], where experimental observations and linear stability analysis on the mean flow were confronted. There, it was shown that the change of the Reynolds number does not substantially change the amplification of the related instability. However, the position of the density gradient relative to the velocity gradient was demonstrated to be as relevant as the (global) density ratio for the stability of the flow. This is in agreement with the more general investigation of density stratification on Kelvin-Helmholtz instabilities conducted by Fontane and Joly [24]. There, it was similarly shown that the density ratio, as well as the collocation of density and velocity gradients, are the governing parameters for the change of the growth rates.

The present investigation of schlieren images at increasing Reynolds numbers shows that the emerging small-scale turbulence affects the density contrast at the interface between the heated breakdown bubble and the jet. The increasing turbulent diffusion flattens the density gradient and shifts it towards the low-density side. This is not visible from the mean temperature profiles since they are governed by the large scale perturbations in the flow. The difference between averaged and instantaneous temperature gradients of the investigated flow is further discussed in the course of a related BOS tomography [21].

4.2. Spatial structures of FTLE and schlieren

The observation of the temporal PVC dynamics reveals that there is no constant amplitude that changes according to the operating conditions. It is a perturbed intermittent oscillation that only reveals a change of the dynamics from a statistical analysis of the observations. In this context, the FTLE structures constitute prototype coherent structures that represent only the phase-averaged flow state.

The experimental smoke and schlieren visualisations contain all sorts of temporal and spatial variations of the structures. The agreement of some instantaneous experimental observations with the FTLE visualisations indicates that the phase averaged shape is characteristic for the underlying coherent structure. However, the turbulent dispersion and diffusion must be kept in mind when comparing it to instantaneous realisations of the flow.

The comparison of the experimental visualisations and the FTLE images shows that simplified perception of the flow as mean flow and the dominant oscillatory motion is sufficient to describe the large scale mixing in the flow. The FTLE computations are based on this basic flow model and they accurately reproduce the instantaneous interfaces between the jet and the breakdown bubble as well as between the jet and the ambient. The undisturbed structure in the FTLE images gives a clear picture of the flow dynamics and allows a better understanding of the mixing processes.

4.3. Observation of stable modes in a turbulent flow

The description of the dynamics by the stochastic amplitude equation explains why the PVC is always observed in measurement data, no matter if the related global mode is stable or unstable. The essential feature of the stochastic model is that it never settles to a stable state. Due to the stochastic forcing, it is always perturbed but it seeks to return to the stable state due to the deterministic dynamics. Therefore, the model responds with oscillatory dynamics to the broadband excitation. These noise-induced oscillations may vary with the noise level, which leads to coherence resonance in certain systems Gang et al. [15]. For

experimental investigations, this implies that the observation of a dominant mode in the data does not mean that the extracted structure belongs to an unstable mode of the flow. There can be slightly damped modes that become excited by the turbulent perturbations.

The operation parameters for the PIV measurements were selected according to the observation of a low amplitude PVC in the measurements. The subsequent reduction of the PVC due to the heating showed a dependence but no clear transition from stable to unstable conditions was attained. The broad scan of operation conditions by pressure measurements revealed that the PIV investigations were conducted only at stable conditions.

This work suggests that the stationary PDF of the oscillation magnitude from (non-time-resolved) PIV measurements can be used as an indicator for the flow state. The PDFs of stable and unstable modes differ mainly in the range near zero. Stable modes show a Rayleigh distribution with nearly linear decay of the function towards zero, while unstable modes have an exponential decay towards zero. The determination of the actual amplification rate needs the knowledge of the noise properties as well, but the sign of the amplification rate depends only on the shape of the PDF.

5. Summary and Conclusions

In the present study, the effect of local heating inside the breakdown bubble on the global mode of the swirling jet was investigated. Motivated by the observations in swirl-stabilised burners, the suppression of the global mode by density stratification was examined. Concerning the combustion studies, the global mode is referred to as precessing vortex core (PVC). The application of electric heating allowed to replicate the suppression of the PVC in a generic swirling jet, as already shown in a previous study. Further effects, such as the observation of a weak PVC at stable conditions and the disappearance of the density dependence at higher Reynolds numbers remain unclear. The present study employs a stochastic model to describe the experimental observations, which further allows characterising the stability margin that marks the transition from a stable to an unstable flow state. The investigation of visualisations from finite-time Lyapunov exponents (FTLE) and experimental schlieren visualisations further detailed the mixing due to the PVC and the dependency on the Reynolds number.

The calibration of the stochastic model using pressure measurements over a wide range of operating conditions allowed to describe the stability margin as a function of the swirl number, the density ratio, and the Reynolds number. The applied heating of the breakdown bubble shifts the bifurcation point towards larger swirl numbers, showing that the density ratio is a second control parameter for the PVC. This dependency vanishes at larger Reynolds numbers, where the stability margin depends only on the swirl number.

The strong influence of the Reynolds number on the stability of the heated flow is attributed to the occurrence of small-scale mixing that smears the sharp density interface. The global density ratio, which is considered as a sole control parameter in the current study, is not sufficient to characterise the influence of density stratification on the PVC. The collocation of density and velocity gradients and the instantaneous density gradient must be considered as well.

The present investigations provide a detailed view of the dynamics of a hydrodynamic instability in a turbulent flow. The stability margin of the flow is identified although the flow is strongly perturbed by turbulent fluctuations at all scales. The proposed procedure needs only measurements from the stationary flow state, no transient or forced experiments are required. This may serve as an example for the investigation of instabilities in other flows. Furthermore, the extraction of FTLE images from non-time-resolved PIV measurements outlines a way for the computation of valuable flow visualisations from limited experimental data.

Acknowledgment

The authors kindly acknowledge the funding from the German Research Foundation under DFG Project PA 920/30-1 and DFG Project PA 920/37-1.

References

[1] N. Syred, J. M. Beér, Combustion in swirling flows: A review, Combustion and Flame 23 (1974) 143–201. doi:10.1016/0010-2180(74)90057-1.

[2] P. Billant, J.-M. Chomaz, P. Huerre, Experimental study of vortex breakdown in swirling jets, Journal of Fluid Mechanics 376 (1998) 183–219. doi:10.1017/S0022112098002870.

[3] F. Gallaire, J.-M. Chomaz, Mode selection in swirling jet experiments: a linear stability analysis, Journal of Fluid Mechanics 494 (2003) 223–253. doi:10.1017/S0022112003006104.

[4] H. Liang, T. Maxworthy, An experimental investigation of swirling jets, Journal of Fluid Mechanics 525 (2005) 115–159. doi:10.1017/S0022112004002629.

[5] K. Oberleithner, M. Sieber, C. N. Nayeri, C. O. Paschereit, C. Petz, H.-C. Hege, B. R. Noack, I. Wygnanski, Three-dimensional coherent structures in a swirling jet undergoing vortex breakdown: stability analysis and empirical mode construction, Journal of Fluid Mechanics 679 (2011) 383–414. doi:10.1017/jfm.2011.141.

[6] M. Stöhr, I. Boxx, C. D. Carter, W. Meier, Experimental study of vortex-flame interaction in a gas turbine model combustor, Combustion and Flame 159 (2012) 2636–2649. doi:10.1016/j.combustflame.2012.03.020.

[7] S. Terhaar, T. G. Reichel, C. Schrödinger, L. Rukes, C. O. Paschereit, K. Oberleithner, Vortex breakdown types and global modes in swirling combustor flows with axial injection, Journal of Propulsion and Power 31 (2014) 219–229. doi:10.2514/1.B35217.

[8] K. Oberleithner, S. Terhaar, L. Rukes, C. Oliver Paschereit, Why nonuniform density suppresses the precessing vortex core, Journal of Engineering for Gas Turbines and Power 135 (2013). doi:10.1115/1.4025130.

[9] L. Rukes, M. Sieber, C. O. Paschereit, K. Oberleithner, The impact of heating the breakdown bubble on the global mode of

a swirling jet: Experiments and linear stability analysis, Physics of Fluids 28 (2016). doi:10.1063/1.4963274.

[10] L. Rukes, M. Sieber, C. O. Paschereit, K. Oberleithner, Methods for the extraction and analysis of the global mode in swirling jets undergoing vortex breakdown, Journal of Engineering for Gas Turbines and Power 139 (2016) 022604. doi:10.1115/1.4034315.

[11] N. Noiray, B. Schuermans, Deterministic quantities characterizing noise driven hopf bifurcations in gas turbine combustors, International Journal of Non-Linear Mechanics 50 (2013) 152–163. doi:10.1016/j.ijnonlinmec.2012.11.008.

[12] N. Noiray, Linear growth rate estimation from dynamics and statistics of acoustic signal envelope in turbulent combustors, Journal of Engineering for Gas Turbines and Power 139 (2017) 041503. doi:10.1115/1.4034601.

[13] M. Lee, Y. Zhu, L. K. B. Li, V. Gupta, System identification of a low-density jet via its noise-induced dynamics, Journal of Fluid Mechanics 862 (2019) 200–215. doi:10.1017/jfm.2018.961.

[14] M. Sieber, C. O. Paschereit, K. Oberleithner, Stochastic modelling of a noise-driven global instability in a turbulent swirling jet, Journal of Fluid Mechanics 916 (2021) A7. doi:10.1017/jfm.2021.133.

[15] Gang, Ditzinger, Ning, Haken, Stochastic resonance without external periodic force, Physical review letters 71 (1993) 807–810. doi:10.1103/PhysRevLett.71.807.

[16] L. Kabiraj, R. Steinert, A. Saurabh, C. O. Paschereit, Coherence resonance in a thermoacoustic system, Physical review. E, Statistical, nonlinear, and soft matter physics 92 (2015) 042909. doi:10.1103/PhysRevE.92.042909.

[17] V. Gupta, A. Saurabh, C. O. Paschereit, L. Kabiraj, Numerical results on noise-induced dynamics in the subthreshold regime for thermoacoustic systems, Journal of Sound and Vibration 390 (2017) 55–66. URL: https://www.sciencedirect.com/science/article/pii/S0022460X16307167. doi:https://doi.org/10.1016/j.jsv.2016.12.004.

[18] Y. Zhu, V. Gupta, L. K. B. Li, Coherence resonance in low-density jets, Journal of Fluid Mechanics 881 (2019) 55. doi:10.1017/jfm.2019.782.

[19] G. Haller, Lagrangian coherent structures, Annual Review of Fluid Mechanics 47 (2015) 137–162. doi:10.1146/annurev-fluid-010313-141322.

[20] M. Sieber, F. Ostermann, R. Woszidlo, K. Oberleithner, C. O. Paschereit, Lagrangian coherent structures in the flow field of a fluidic oscillator, Phys. Rev. Fluids 1 (2016) 050509. doi:10.1103/PhysRevFluids.1.050509.

[21] H. M. Lang, K. Oberleithner, C. O. Paschereit, M. Sieber, Measurement of the fluctuating temperature field in a heated swirling jet with bos tomography, Experiments in Fluids 58 (2017) 88. doi:10.1007/s00348-017-2367-1.

[22] F. Lückoff, M. Sieber, C. O. Paschereit, K. Oberleithner, Impact of the precessing vortex core on nox emissions in premixed swirl-stabilized flames - an experimental study, Proceedings of ASME Turbo Expo 2020 (2020).

[23] J. Reinaud, L. Joly, P. Chassaing, The baroclinic secondary instability of the two-dimensional shear layer, Physics of Fluids 12 (2000) 2489. doi:10.1063/1.1289503.

[24] J. Fontane, L. Joly, The stability of the variable-density kelvin–helmholtz billow, Journal of Fluid Mechanics 612 (2008) 237–260. doi:10.1017/S0022112008002966.

[25] L. Rukes, M. Sieber, C. O. Paschereit, K. Oberleithner, Effect of initial vortex core size on the coherent structures in the swirling jet near field, Experiments in Fluids 56 (2015) 183. doi:10.1007/s00348-015-2066-8.

[26] J. S. Müller, F. Lückoff, P. Paredes, V. Theofilis, K. Oberleithner, Receptivity of the turbulent precessing vortex core: synchronization experiments and global adjoint linear stability analysis, Journal of Fluid Mechanics 888 (2020).

[27] C. E. Willert, M. Gharib, Digital particle image velocimetry, Experiments in Fluids 10 (1991). doi:10.1007/BF00190388.

[28] G. S. Settles, Schlieren and shadowgraph techniques: Visualizing phenomena in transparent media, Experimental Fluid Mechanics, Springer, Berlin and Heidelberg and New York, 2001. doi:10.1007/978-3-642-56640-0.

[29] L. Sirovich, Turbulence and the dynamics of coherent structures: Part i: Coherent structures, Quarterly of Applied Mathematics 45 (1987) 561–571.

[30] F. Lückoff, M. Sieber, C. O. Paschereit, K. Oberleithner, Phase-opposition control of the precessing vortex core in turbulent swirl flames for investigation of mixing and flame stability, Journal of Engineering for Gas Turbines and Power 141 (2019). doi:10.1115/1.4044469.

[31] R. Sonnenberger, K. Graichen, P. Erk, Fourier averaging: a phase-averaging method for periodic flow, Experiments in Fluids 28 (2000) 217–224. doi:10.1007/s003480050381.

[32] J. D'Errico, Surface fitting using gridfit, matlab central file exchange, 2006.

[33] L. D. Landau, On the problem of turbulence, C. R. Acad. Sci. URSS 44 (1944).

[34] J. B. Roberts, P. D. Spanos, Stochastic averaging: An approximate method of solving random vibration problems, International Journal of Non-Linear Mechanics 21 (1986) 111–134. doi:10.1016/0020-7462(86)90025-9.